

# Adapted Fast Gradient Projection Algorithm for Magnetic Resonance Image Denoising

Manar A. Al-Abaji<sup>1,\*</sup> and Zohair Al-Ameen<sup>2</sup>

<sup>1</sup> Department of Computer Science, College of Education for Pure Science, University of Mosul, Nineveh, Iraq

<sup>2</sup> ICT Research Unit, Computer Center, University of Mosul Presidency, University of Mosul, Nineveh, Iraq

Email: manar\_alabaji@uomosul.edu.iq (M.A.A.-A.); qizohair@uomosul.edu.iq (Z.A.-A.)

\*Corresponding author

**Abstract**—The critical objective of image denoising is to provide a visually appealing image that maintains the essential features of its noisy equivalent. Magnetic Resonance (MR) images are acquired with degradations, and a common deterioration is Rician noise, which arises from variations in temperature or technical faults. Random noise reduces the clarity of images and raises the risk of incorrect diagnosis because it potentially conceals critical anatomical features and important diagnostic observations. Denoising optimizes the visibility of subtle lesions by minimizing noise and increasing diagnostic precision and sensitivity. Various existing denoised methods fail to attenuate the noise properly, leading to blurring or removing fine details from the processed images. Thus, this study proposes an Adapted Fast Gradient Projection (AFGP) algorithm for MR image denoising. The proposed algorithm can automatically compute the regularization parameter for each MR image via the local image information. Moreover, a detail-emphasized phase is applied at each iteration to maintain the structure and delicate features. The performance of the proposed AFGP algorithm is assessed with a dataset of real noisy images, compared with various denoising algorithms, and the results are evaluated using three sophisticated accuracy methods in addition to runtime. Ultimately, the proposed approach yielded satisfactory outcomes, surpassing all comparable techniques with relatively fast runtimes.

**Keywords**—Magnetic Resonance Images (MRI), denoising, Rician

## I. INTRODUCTION

Magnetic Resonance Imaging (MRI) is an essential imaging modality that enables superior visualization of human tissue and organs [1]. The accuracy of medical diagnosis and computerized evaluation, such as classification, segmentation, and registration, is heavily influenced by the quality of the MRI image [2]. MRI images can experience degradation, including Rician noise, due to temperature variations and hardware issues [3]. This degradation results in the loss of fine details, hampers the extraction of useful information, and poses challenges for automated computerized assessments [2]. The denoising process is challenging in

image processing due to the hurdles of preserving image information such as texture, edges, and small features to achieve a high-quality output [4]. The primary objective of image denoising is to acquire a visually appealing image that retains the maximum level of detail from its noisy counterpart. Hence, the primary criterion for any image denoising technique is to attenuate the noise while maintaining the delicate features and edges without introducing unwanted artifacts [5].

Rician noise is a known type of noise that greatly obscures the vitality details in MRI images, and developing an effective denoising algorithm is a significant challenge. Despite various denoising concepts, most still need to reach a satisfactory level in practice due to the high computational cost, blurring, unwanted flaws generation, and the removal of small image details [6]. In MR images, noise can be reduced on both the hardware and software levels. At a hardware level, the noise is reduced by enhancing the performance of the MRI scanning equipment. In contrast, the software level utilizes an algorithm-based way to process the acquired data, offering a viable and efficient approach to attenuate the noise [7].

Bilateral filtering is an image-smoothing approach that maintains the edges' strength. Originating in 1995, the research conducted by Aurich and Weule on nonlinear Gaussian filters marked the beginning of this field. Smith and Brady subsequently rediscovered it as a component of their SUSAN framework, and after that, Tomasi and Manduchi gave it its present name. Since then, bilateral filtering usage has experienced fast growth and is currently widespread in image-processing applications. Due to its output being a weighted average of its inputs, this filter is classified as a nonlinear smoothing technique. Furthermore, it operates identically to Gaussian convolution by generating a weighted pixel average. Yet, the distinction lies in the fact that this filter has considered variations in intensity to maintain the sharpness of edges and intricate features. A key benefit of the bilateral filter is its ability to determine the similarity between two pixels by assessing their spatial distance and the similarity of their intensity levels [8].

The Total Variation (TV) concept has been broadly used to address several imaging challenges, including image denoising. It was first introduced by Rudin, Osher,

Manuscript received August 6, 2024; revised September 4, 2024; accepted September 26, 2024; published March 14, 2025.

and Fatemi in 1992. The primary purpose of the TV concept is to attenuate the image noise. It aims to identify the variation in intensity (energy) between adjacent pixels and then reduce it by utilizing an iterative optimization method, where the denoised image is updated repeatedly until it meets a specified condition. This task is achieved by minimizing TV and the discrepancy between the input noisy and denoised images [5]. The Fast Gradient Projection (FGP) method is a rapid optimization approach that utilizes gradients and TV to solve denoising issues. It was first proposed by Beck and Teboulle in 2009 [9] to address optimization challenges related to constraints. The FGP method may effectively reduce the variations while guaranteeing the denoised image meets specific constraints, such as similarity in details to the noisy input image.

Traditional optimization strategies are computationally intensive for large-size images. Accordingly, the FGP method is beneficial since it utilizes gradient information and projects it onto a viable set while updating the denoised image, offering rapid convergence [9]. Still, FGP tends to over-smooth the MRI image, leading to the loss of small image details. It also uses a constant regularization parameter ( $\lambda$ ), and choosing a suitable value of  $\lambda$  for every image is uneasy. Therefore, this paper presents an adapted Fast Gradient Projection (AFGP) algorithm to denoise MRI images while maintaining the tiny features without excessive smoothing or blurring of the results. The designed AFGP has two clearly defined stages. Firstly, each iteration includes a detail-emphasis phase to augment the high-frequency components. A second method involves the automated calculation of  $\lambda$  using the image's local information. The main contributions of this study are the following: (i) rely on image information to calculate  $\lambda$  automatically. (ii) optimize the algorithm by reducing the number of required parameters. (iii) A low-complexity detail-emphasizing step is implemented at each iteration to preserve the small image details and improve the edge representation. By attaining these contributions, better denoising results are obtained. The remaining sections of this research are structured as follows: Section II provides a concise overview of the related work. Section III explains the original and the developed algorithms in detail. Section IV presents the obtained qualitative and quantitative results, demonstrating the performances of the proposed algorithm against other algorithms. Section 5 provides the final inference and conclusions.

## II. LITERATURE REVIEW

Over the past several years, many denoising algorithms with dissimilar notions have been introduced. In 2014, a Weighted Nuclear Norm Minimization (WNNM) algorithm was presented [10]. It utilized an iterative optimization approach to identify the solution that minimizes the weighted nuclear norm of a matrix, which represents the underlying structure of the image being denoised. However, this method needs more adaptability to filter single values, reducing its applicability and affecting the denoising capabilities because of its

ineffectiveness in capturing the subtle characteristics of real-world images. In 2015, a trilateral filter was introduced [11]. This filter utilizes a Rough Set Theory (RST) to generate edge maps and class labels at a pixel level. These maps and labels are then employed to enhance the effectiveness of bilateral filters. However, RST may have difficulties dealing with complex noise patterns frequently found in real-world images. Moreover, it may require significant computational costs, especially when dealing with high-resolution images, leading to long processing times.

In 2016, a nonlocal self-similarity and Low-Rank Approximation (LRA) algorithm was developed [12]. It approximates group matrices using the block-matching technique and Singular Value Decomposition (SVD), keeping just a small number of critical singular values and their accompanying vectors. This approach uses the optimum energy compaction aspect of SVD. However, it lacks generality and may exhibit suboptimal performance when the noise characteristics stray substantially from the assumptions inherent to the methodology. In 2018, a new method was reported that utilizes Second-order Non-convex Total Variation (SNTV) [13]. The model efficiently minimizes the staircase artifact by exploiting the benefits of higher-order non-convex regularization and overlapping group sparsity regularization. However, it must balance minimizing noise and maintaining the image information, as over-denoising can occur and remove the small image details.

In 2019, a Statistical Nearest Neighbors (SNN) concept was introduced [14]. In SNN, the selection of neighbors depends on how close their squared distance from the reference patch is to its expectation. This reduces the noise-free patch prediction error estimation, which enhances image quality and minimizes the computational costs more than the traditional nearest neighbors approach. However, SNN has a limitation in preserving image information, causing detail blurring in the low-contrast image when denoising using more than one NN. Moreover, it may not offer a conception of the optimal number of neighbors needed for various types of images or noise levels. In 2019, an Iterative Mean Filter (IMF) was presented [15]. In the IMF framework, the approach analyzes a specific window of pixels with a set size of  $3 \times 3$ . Instead of using the median value, it calculates the constrained mean of the window to determine the new gray value for the central pixel. However, it is constrained with a fixed-size window, which may need help to adapt to varying noise densities across different regions of an image, potentially leading to suboptimal denoising outcomes in areas with significant noise characteristics.

In 2020, an Adaptive Total Variation (ATV) based algorithm was proposed [16]. It helpfully attenuates noise and maintains the image structures. Its drawback is the intricacy involved in selecting parameters. Inadequate choice of parameters may result in better-quality outcomes. Furthermore, the adaptive multiscale parameter estimation and inverse gradient computations are accompanied by computational complexity,

potentially leading to longer processing times for large-scale images. In 2021, a Variational Mode Decomposition (VMD) based algorithm was delivered [17]. This approach efficiently exploits VMD principles to improve quality by reducing the intensity of rician noise. However, in addition to this technique's computational complexity, its processing abilities depend on multiple essential variables, making the selection of parameters more challenging.

In 2021, a fuzzy-based non-local mean filter was introduced [18]. This filter detects non-local comparable pixels by employing a specific fuzzy function. Consequently, these corresponding pixels are utilized to create pixels devoid of noise. A significant limitation of this technology is the improper restoration of structural information from a noisy image. In 2022, a score-based reverse diffusion sampling concept was presented [19]. It utilizes a deep neural network model for the denoising process as well. However, the reverse diffusion mechanism is inherently slow, requiring several iterations through the neural network to get optimal outcomes, resulting in high processing times. In 2023, an enhanced intuitionistic fuzzy adaptive filter was introduced [20]. The model filters through pixel categorization into membership and non-membership grades. It also improves the quality and edges by enhancing the contrast via histogram equalization, yet processing takes longer than traditional filters. In 2023, two deep learning frameworks, ResNet50 and Inception V3, were presented in [21]. These frameworks are specifically designed to classify brain MRI images. This work integrates fundamental methodologies, including early stopping and reduce LR on plateau, to enhance the models through hyperparameter optimization. This approach involves augmenting the model by developing additional layers to improve performance.

In 2024, a Morphological Component Analysis (MCA) based model was delivered [22]. It applies the variance-stabilizing transformation to reduce the noise and preserve details. Moreover, by setting an adaptive threshold, the MCA concept is used to handle the interference between the noise and the valuable information. Although this method well-preserved textural details, it faces challenges when handling high noise levels. In 2024, a particle swarm optimization based on a principal component analysis algorithm is presented [23]. It traverses the intensities of pixels, reduces the calculations, and expands the search volume to cover the entire image to deliver more efficient denoising. This method uses a Rician noise level approximation model that can affect the denoising abilities and result in suboptimal results. Previous studies have shown that various concepts have been utilized, ranging from simple to complex, with different computational costs. Still, most of these algorithms have drawbacks, and the opportunities remain to develop a

new algorithm that is fast and reliable, preserving edges and small image information more efficiently.

### III. RESEARCH METHOD

#### A. Proposed Algorithm

The main aim is to adapt the original FGP algorithm to handle the regularization parameter ( $\lambda$ ) issues and excessive smoothing. This section explains the original FGP algorithm [9], and then the performed modifications are given in detail. The original FGP aims to progressively attenuate the image noise by employing gradient projection and acceleration models to achieve the needed convergence. Accordingly, it utilizes an accelerated gradient descent approach to iteratively update the gradient and applies projection to preserve constraints. This process finally reconstructs a denoised image by reducing the total variations. The output denoised image  $x$  is computed by subtracting the regularized gradient from the input noisy image  $y$ . This phase converts the most beneficial gradient in the direction to the original variable using the following approach:

$$(p_k, q_k) = P_c \left[ (r_k, s_k) + \left( \frac{1}{8\lambda} \right) D^T (P_c [y - \lambda D(r_k, s_k)]) \right] \quad (1)$$

$$t_{k+1} = \frac{1 + \sqrt{1 + 4t_k^2}}{2} \quad (2)$$

$$(r_{k+1}, s_{k+1}) = (p_k, q_k) + \left( \frac{t_k - 1}{t_{k+1}} \right) (p_k - p_{k-1}, q_k - q_{k-1}) \quad (3)$$

where  $\lambda$  is the Regularization parameter;  $D$  is the differential method, which calculates the gradient of the image;  $D^T$  is the adjoint of  $D$ ; The expression  $(1/8\lambda)$  serves as a scaling factor to normalize the step size along the gradient ascent direction, which is chosen to ensure the FGP algorithm better converges;  $(p_k, q_k)$  represents the current estimation of the denoised image's gradient, and its calculation includes the gradient descent step followed by the projection step onto the feasible set  $c$  as described in Eq. (1).  $t_{k+1}$  is the updated momentum parameter that controls the influence of the previous update;  $(r_k, s_k)$  denotes an auxiliary variable, which is updated in each iteration to accelerate the FGP convergence by using the momentum parameter to combine the current estimation of the denoised image's gradient and its previous estimation. The output denoised image is computed using the following equation:

$$x = P_c (y - \lambda D(p_k, q_k)) \quad (4)$$

To know the denoising abilities of the original FGP algorithm, it was applied to various real-degraded MR images, and samples of the attained results are given in Fig. 1.

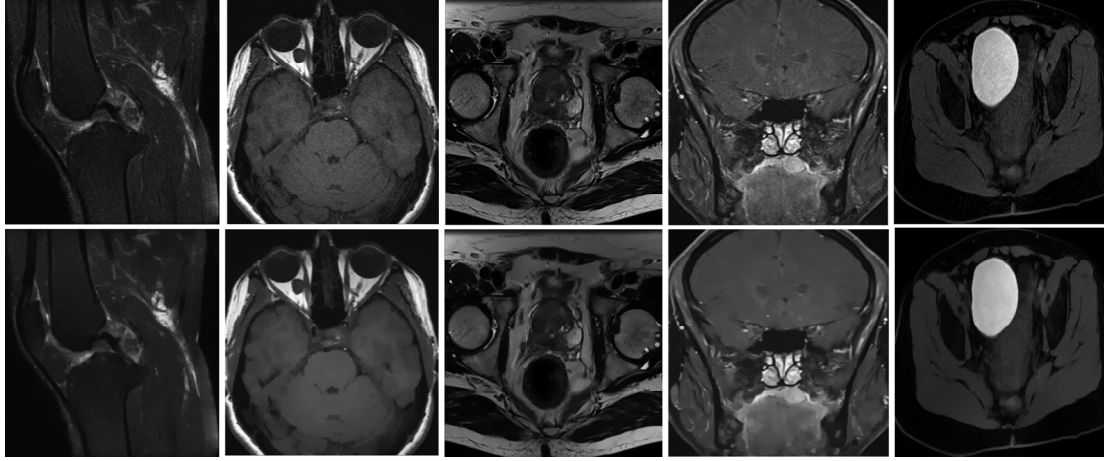


Fig. 1. Processing real-degraded MR images with the original FGP algorithm. 1st row: Real-noisy MR image; 2nd row: Denoised using the original FGP.

The images processed using the original FGP algorithm exhibit unbalanced noise attenuation with apparent smoothness and blurring effects. This can remove small yet crucial medical information, leading to undesirable quality results. Still, the FGP has a low computational cost, pinpointing its vast development potential to enhance its processing abilities. Thus, an Adapted Fast Gradient Projection (AFGP) algorithm is introduced, aiming to denoise degraded MR images efficiently while preserving the minor details without over-smoothing or blurring the results. The developed AFGP includes two distinct modifications. The first is utilizing a detail-emphasis step in each iteration to enhance the high-frequency elements. The second is computing  $\lambda$  automatically using the image's local information since  $\lambda$  value balances the trade-off between detail preservation and noise attenuation, in that a lower value keeps the noise and preserves more details while a higher value performs the opposite.

As mentioned earlier, the value of  $\lambda$  dramatically influences the performance of FGP, and the main aim here is to achieve a good balance between the impact of the fidelity term and the regularization term in TV on the calculated solution [24]. A direct relationship exists between the standard deviation ( $\sigma$ ) and the Mean TV norm (MTV) value. It is possible to get an approximate  $\sigma^*$  value from the noisy observation to be utilized in the iterative estimation of  $\lambda$ . Thus, the first step in the AFGP algorithm involves the approximation of  $\lambda$  value based on the MTV notion using the input image  $y$  using the following equations:

$$\text{MTV}(y) = \frac{\text{TV}(y)}{n_1 \cdot n_2} \quad (5)$$

$$\sigma^* = s \cdot \text{MTV}(y) + b \quad (6)$$

$$\lambda = 1.5 \cdot \sigma^* \quad (7)$$

where  $\text{TV}(y)$  is the total variation of image  $y$ , which equals to  $\text{sum}[\text{abs}(D(y))]$ ;  $s$  is a scaling value, which is

initially set to (0.58);  $b$  is a constant value, which is initially set to (0.01);  $\sigma^*$  is sigma approximate value. Throughout the denoising process, the value of  $\lambda$  updates iteratively based on the MTV of the updated result ( $r_k, s_k$ ) using the following equations:

$$\text{MTV}(r_k, s_k) = \frac{\text{TV}(r_k, s_k)}{n_1 \cdot n_2} \quad (8)$$

$$\eta = \eta + 0.003 \quad (9)$$

$$\sigma^* = s \cdot \text{MTV}(r_k, s_k) + b \quad (10)$$

$$\lambda = (d + |\eta|) \cdot \sigma^* \quad (11)$$

where  $d$  is a constant value, set to (0.35);  $\eta$  is a small constant, initiated at zero and updated at each iteration to activate  $\lambda$  better;  $s$  and  $b$  are also constant values, set to 0.58 and 0.01, respectively;  $n_1$  and  $n_2$  are image dimensions. A detail-emphasis step is applied at each iteration to overcome the loss of minor details and enhance the high-frequency elements. To perform that, an initial step before the iteration loop is implemented involves smoothing the image  $y$  with the classical bilateral filter to produce the smoothed image (BF). During the iterations, BF is subtracted from the estimated image at each iteration to obtain the highlights image. The output is added back to the estimated image to emphasize the details. At the first iteration, ( $x_{\text{prev}} = \text{BF}$ ), the detail emphasizes step can be done iteratively using the following equations:

$$x = (y - \lambda D(p_k, q_k)) \quad (12)$$

$$x = x + (x - x_{\text{prev}}) \quad (13)$$

$$x_{\text{prev}} = x \quad (14)$$

Adding the two above modifications to adapt the algorithm allows a balance between details preservation and denoising power to be performed, benefiting in avoiding the over-smoothing effect and reducing the blur artifact while keeping the minor details and semi-automating the algorithm. In addition, these modifications allowed faster convergence, leading to less iteration utilization and quicker production of the output image.

#### B. Experiment Setup and Evaluation Criteria

This section presents the necessary empirical preparation to apply the developed AFGP algorithm and validate its efficiency. The algorithm's performance is assessed using real-noisy images obtained from <https://www.ctisus.com/>, which is deemed one of the leading websites for radiological images administrated by the School of Medicine at Johns Hopkins. To assess the visual quality of denoised images, the Perception-based Image Quality Evaluator (PIQE) [25], Blind/Referenceless Image Spatial Quality Evaluator (BRISQUE) [26], and Naturalness Image Quality Evaluator (NIQE) [27] metrics were selected. The PIQE metric relies on the local features to predict quality and measures the visibility of distortion in the image without requiring any training data. The BRISQUE metric consists of two steps. The first involves extracting entropy and energy features using Gabor filters, while the second determines parameters to assess the quality using the linear least squares model. BRISQUE measures the perceptual quality of the image. The NIQE measures the naturalness by evaluating the deflection from statistical patterns in natural images. The distorted image quality is determined by measuring how the distorted image differs from the statistical properties of the model. A lower score indicates better performance for all metrics, i.e., less distortion visibility for PIQE, better best perceptual quality for BRISQUE, and better naturalness for NIQE. All

algorithms were implemented using MATLAB R2023a on a laptop with an Intel Core i7-10510U CPU and 16 GB of RAM.

## IV. RESULT AND DISCUSSION

#### A. Experiment Results

In the following part, we conduct experiments on real-noisy images from the Ctisus dataset to show the performance of the developed AFGP algorithm in MRI image denoising. Figs. 2–5 depict the original distorted MRI images and their denoised observations using the proposed AFGP algorithm. In all experiments, we use fixed parameter values which were taken from the ranges established by Wang *et al.* [28], to direct our selection procedure in this study. Although that study proposed several values for each parameter, we chose to concentrate on a singular value for each parameter, considering our particular circumstances and the effectiveness of the achieved outcomes. Through intensive experimentation, we have determined that a scaling value ( $s$ ) of 0.58, a constant value ( $b$ ) of 0.01, lambda of  $1.5 \times \sigma^*$ , and ( $d$ ) of 0.35 resulted in the highest performance in our MRI denoising tasks. The decision was taken to achieve a satisfactory compromise between computational efficiency and denoising quality, guaranteeing optimal outcomes while reducing processing time.

From Figs. 2 to 5, the images denoised by the AFGP algorithm exhibited acceptable details, as the apparent noise is effectively attenuated without massively blurring the results while preserving the minor information from being removed. It was also noticed that the AFGP algorithm can work with different types of MR images and successfully attenuate noise. This is vital as it is a step in providing efficiency and validating development.

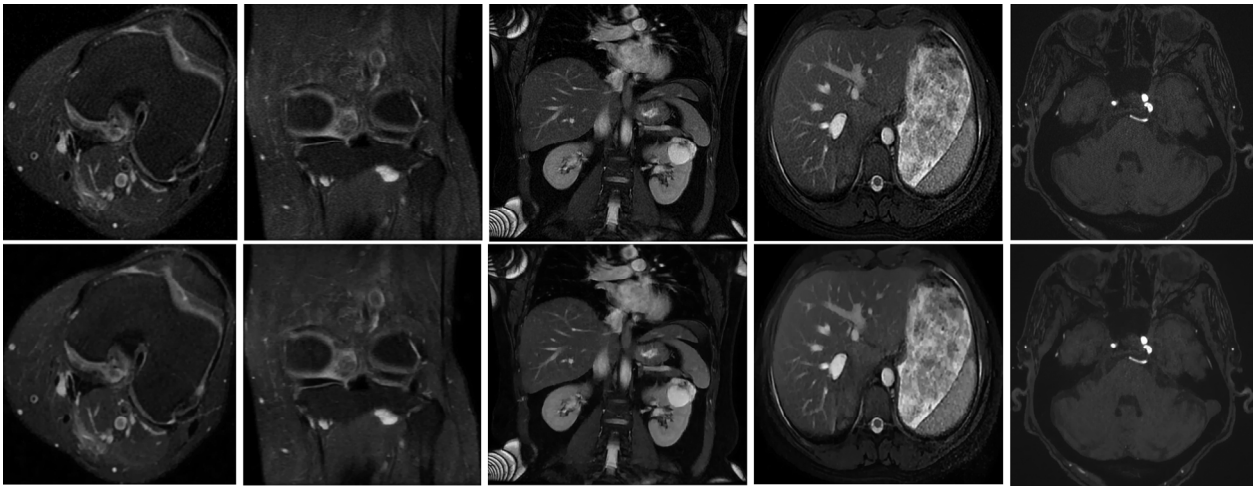


Fig. 2. Top row: Real noisy MRI image; bottom row: Denoised using the proposed algorithm.

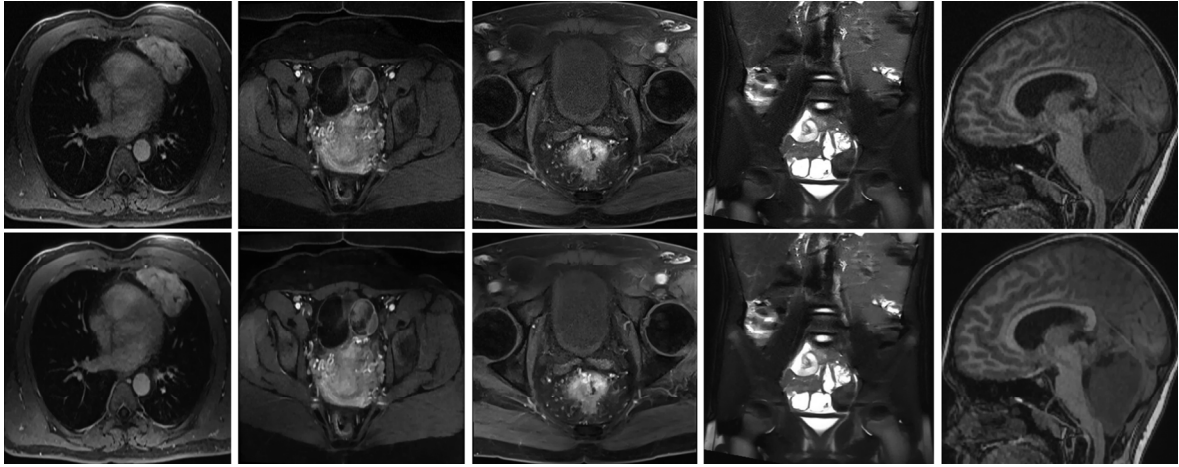


Fig. 3. Top row: Real noisy MRI image; bottom row: Denoised using the proposed algorithm.

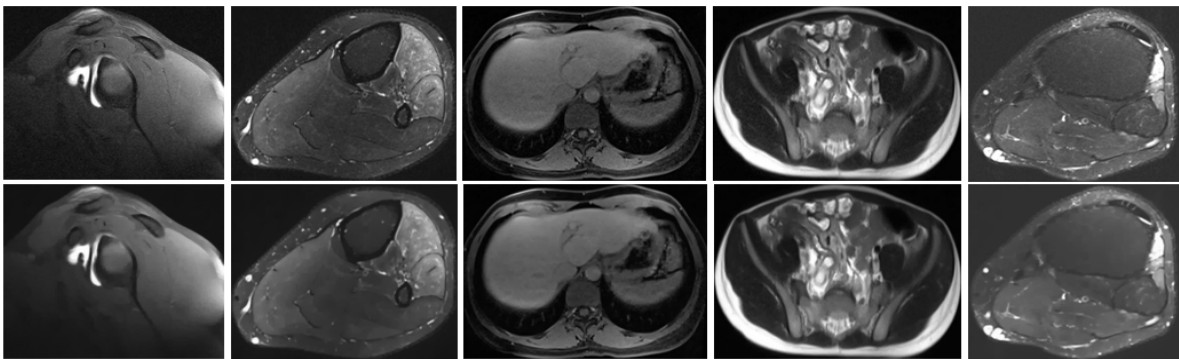


Fig. 4. Top row: Real noisy MRI image; Bottom row: Denoised using the proposed algorithm.

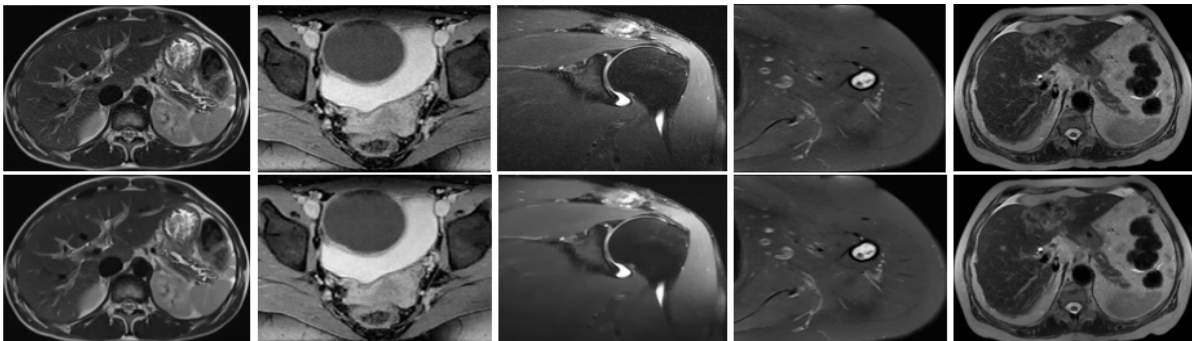


Fig. 5. Top row: Real noisy MRI image; bottom row: Denoised using the proposed algorithm.

### B. Comparison Results and Discussion

The denoising capability of the proposed algorithm is also assessed by comparing it to other existing algorithms, such as the original FGP [9], the Low-Rank Approximation (LRA) [12], Second-order Non-convex Total Variation (SNTV) [13], adaptive total variation (ATV) [16], a Statistical Nearest Neighbors (SNN) [14] and Weighted Nuclear Norm Minimization (WNNM) [10]. Figs. 6 to 9 display the comparison results. Tables I to IV present the recorded accuracy readings and the implementation times. Figs. 10 to 13 show the recorded scores as charts. The comparison results present dissimilar performances obtained through the evaluation scores. The lowest scores in PIQE, BRISQUE, NIQE, and implementation time denote the best performances.

In terms of performance analysis, the original FGP recorded relatively short runtimes; nevertheless, it tended to blur the output noticeably when the noise was reduced, which resulted in a reduction in clarity and a smaller number of details. Because of this, it received an average score in PIQE, high in the BRISQUE, and unacceptable in the NIQE. The SNN method achieved the second slowest processing time and generated abnormal visuals due to visible noise resulting from its failure to denoise the images. Therefore, it achieved the worst NIQE value and displayed high PIQE and BRISQUE values. As for WNNM, although it received a lower NIQE score, it provided relatively blurred results with apparent noise. Therefore, it recorded high PIQE and moderate BRISQUE values and had the longest processing time. As for the LRA method, despite achieving low scores in

PIQE and BRISQUE, a moderate score in NIQE, and a long implementation time, the LRA maintained the edges

and features of the picture without causing considerable blurring. It also offered adequate naturalness.

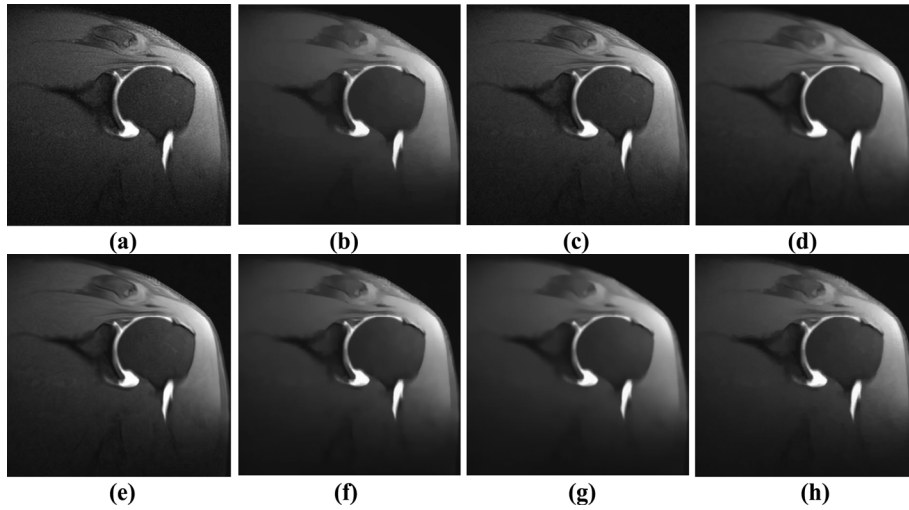


Fig. 6. Comparison results (Part 1): (a) Real noisy image; other images are denoised by (b) Original FGP; (c) SNN; (d) WNNM; (e) LRA; (f) SNTV; (g) ATV; (h) Proposed AFGP.

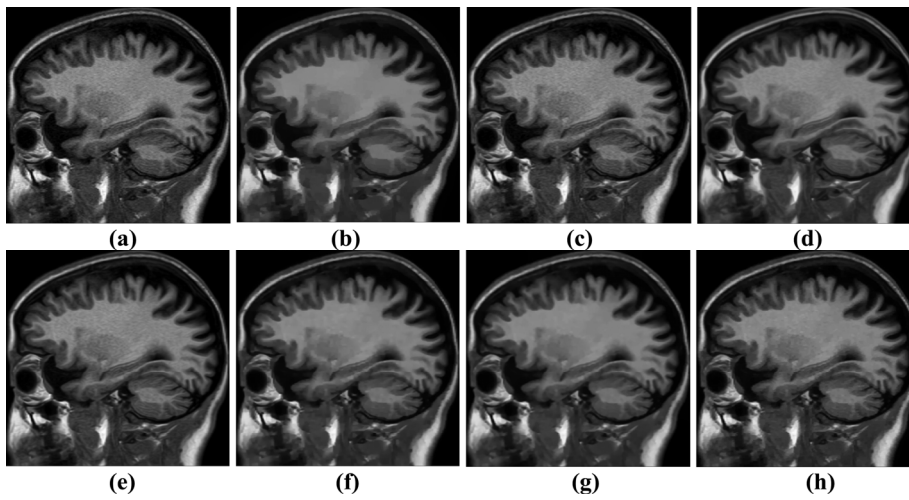


Fig. 7. Comparison results (Part 2): (a) Real noisy image; other images are denoised by (b) Original FGP; (c) SNN; (d) WNNM; (e) LRA; (f) SNTV; (g) ATV; (h) Proposed AFGP.

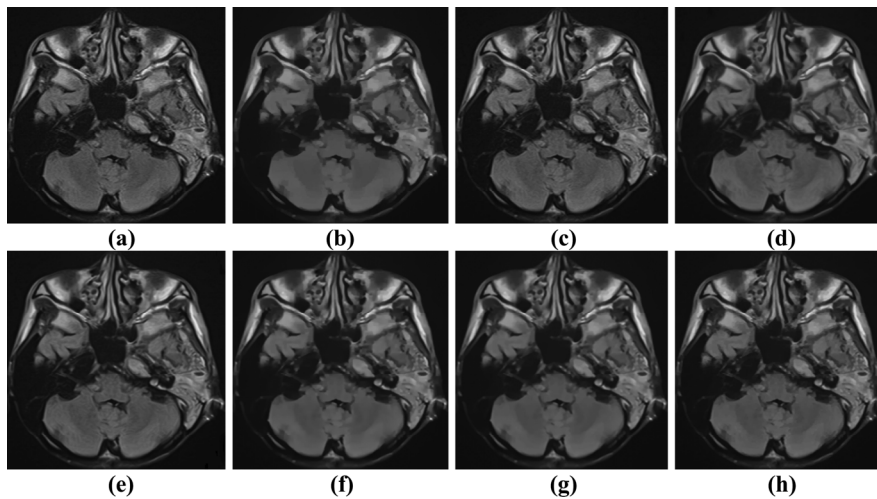


Fig. 8. Comparison results (Part 3): (a) Real noisy image; other images are denoised by (b) Original FGP; (c) SNN; (d) WNNM; (e) LRA; (f) SNTV; (g) ATV; (h) Proposed AFGP.

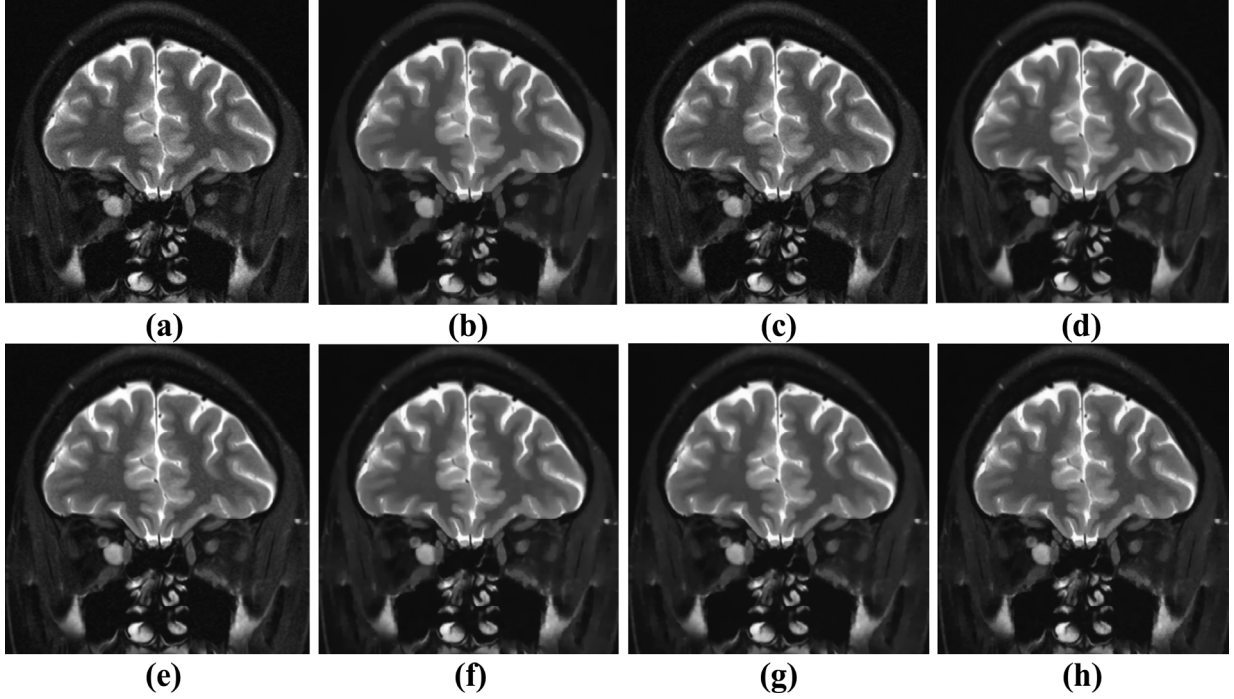


Fig. 9. Comparison results (Part 4): (a) Real noisy image; other images are denoised by (b) Original FGP; (c) SNN; (d) WNNM; (e) LRA; (f) SNTV; (g) ATV; (h) Proposed AFGP.

TABLE I. PIQE ↓ SCORES

Fig.	FGP	SNN	WNNM	LRA	SNTV	ATV	AFGP
4	76.2958	77.2840	76.3482	62.4283	63.3504	93.7900	28.9644
5	90.3729	85.2027	84.2386	84.3028	82.1730	94.3436	48.2884
6	76.6568	86.1273	85.7613	84.3572	84.0107	94.4030	56.6182
7	86.7067	85.1520	85.4231	83.7403	83.1301	92.0210	43.7544
Av.	82.5081	83.4415	82.9428	78.7072	78.1661	93.6394	<b>44.4064</b>

TABLE II. BRISQUE ↓ SCORES

Fig.	FGP	SNN	WNNM	LRA	SNTV	ATV	AFGP
4	49.3106	42.3953	37.7132	39.4671	50.3646	62.6319	40.4242
5	50.5066	58.5388	59.2168	58.6633	46.8095	60.1484	50.5175
6	51.4529	54.3569	55.0226	54.4177	49.8977	49.8204	51.0499
7	52.8846	52.9807	49.3981	48.7911	48.8515	57.2473	46.0833
Av.	51.0387	52.0679	50.3377	50.3348	48.9808	57.4620	<b>47.0187</b>

TABLE III. NIQE ↓ SCORES

Fig.	FGP	SNN	WNNM	LRA	SNTV	ATV	AFGP
4	4.6037	4.5884	4.4862	3.9958	4.4973	4.8122	4.0217
5	5.3681	5.3822	5.5768	5.6561	5.0018	5.3014	4.9690
6	5.7460	5.4906	5.1977	5.4363	5.5766	5.0880	5.2298
7	5.5003	5.7638	4.9509	5.1727	5.1748	5.1107	4.8964
Av.	5.3045	5.3063	5.0529	5.0652	5.0626	5.0781	<b>4.7792</b>

TABLE IV. RUNTIMES ↓ IN SECONDS

Fig.	FGP	SNN	WNNM	LRA	SNTV	ATV	AFGP
4	1.7917	41.2395	57.8590	20.4008	10.4559	17.3704	1.6188
5	6.9486	143.0602	193.8813	69.4522	26.9957	76.9515	5.2180
6	6.4454	132.2607	184.9277	64.4699	26.4337	61.6806	4.7561
7	7.3534	148.7217	203.6490	75.5884	28.0668	60.2748	5.4101
Av.	5.6348	116.3205	160.0792	57.4778	22.9880	54.0693	<b>4.2508</b>

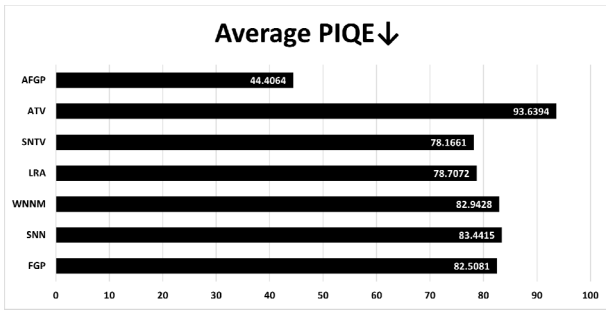


Fig. 10. Chart of the average PIQE values.

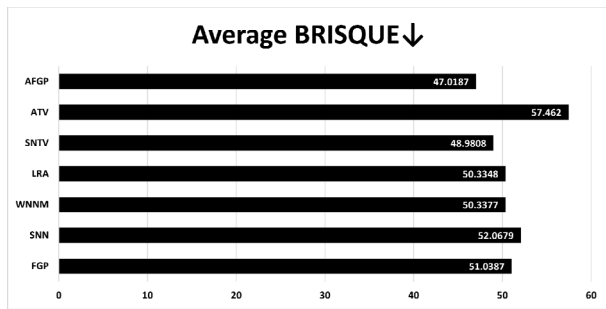


Fig. 11. Chart of the average BRISQUE values.

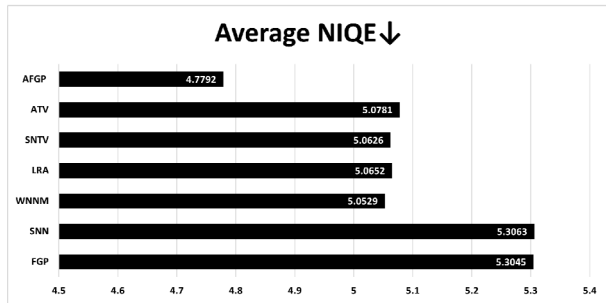


Fig. 12. Chart of the average NIQE values.

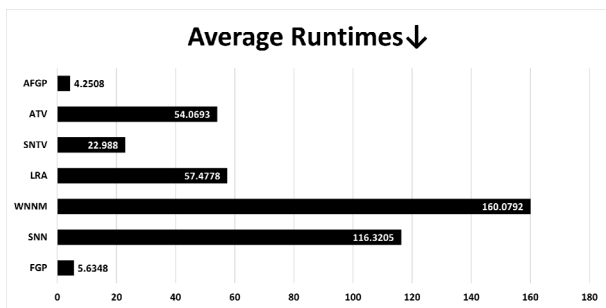


Fig. 13. Chart of the average runtimes.

The SNTV and ATV algorithms rely on the TV concept. SNTV performed better than the ATV regarding average accuracy measures, obtaining lower scores with the three metrics. The SNTV produced images with satisfactory perceptual quality and attenuated the noise properly yet introduced noticeable blurring to the results. Thus, it was recorded as the second-best in PIQE and BRISQUE, with low scores in NIQE. Also, it had a shorter implementation time than the ATV algorithm. The ATV algorithm provided artificial-like results because it introduced over-smoothing, which caused blurring and loss of details. Therefore, it obtains the highest values in PIQE and BRISQUE with high values in NIQE. The proposed AFGP algorithm performed better, recording the lowest in PIQE, BRISQUE, and NIQE, with the fastest implementation times, since the denoised results exhibited more details, retaining almost all the details. Also, although some mathematical computations were added to AFGP, it required lower iterations to reach the desired results, leading to less implementation time. This is important as rapid and effective denoising has been introduced in this study that outperformed many existing algorithms in the field.

C. Statistical Test to Validate the Improvement

Paired statistical tests are the most reasonable method for comparing the efficiency of the two denoising methods. For each metric, to choose which test (t-test or Wilcoxon Signed-Rank) will be implemented to test if the two methods are significantly different in performance, the normality test of the differences between the two methods has been carried out by the Shapiro-Wilk test under the null hypothesis  $H_0$ : the defenses came from a normally distributed population. Since the  $p$ -values corresponding to each metric are less than  $p < 0.05$ , the  $H_0$  will be rejected. In other words, the differences between the pairs in all metrics are not normally distributed. Since a normality assumption is not met, a non-parametric test called the Wilcoxon Signed-Rank test will apply under null hypothesis  $H_0$ : There is no significant difference between the two denoising methods for each metric. Finally, a Cohen test has been carried out to assess the magnitude of the difference between the two methods. Table V below illustrates the corresponding values and p-values values for each metric obtained after denoising the images by the two methods, FGP and AFGP.

TABLE V. ILLUSTRATE THE PAIRED STATISTICAL TESTS OF THE FGP AND AFGP DENOISING PERFORMANCE ACCORDING TO EACH EVALUATION METRIC PIQE, BRISQUE, AND NIQE

Metrics	Shapiro-Wilk		Wilcoxon Signed-Rank				Cohen-d			
	FGP- AFGP		FGP- AFGP		Median of FGP	Median of AFGP	FGP- AFGP		confidence interval 95%	
	Test Value	P-value	Test Value	P-value			d-estimate	Size effect	lower	upper
PIQE	0.97643	4.294e-6*	78577	2.2e-16*	87.01767	53.39911	3.062648	Large	2.8031	3.32210
BRISQUE	0.97078	3.506e-07*	58565	1.4e-15*	51.18949	50.11056	0.4805882	Small	0.3624	0.5986
NIQE	0.99002	0.008115*	80195	2.2e-16*	7.104918	4.962598	4.354305	Large	3.9532	4.7553

Note: \*Since the calculated p-values are less than 0.05, the all-corresponding null hypothesis will be rejected.

First, the  $p$ -values for the three metrics are less than 0.05, which means no evidence that the differences between the methods by the whole metrics came from normal distribution (The null hypothesis was rejected). As for the Wilcoxon Signed-Rank test, the metrics recorded  $p$ -values of less than 0.05. That means there is evidence that differences in the performance between the methods exist, and since the median of the AFGP in the three metrics is less than the median of the FGP, then AFGP outperforms FGP in all metrics. The Cohen-d test estimates the magnitude (size effect) of this performance. According to the d-estimated value of this test, the large impact of the improvement on the FGP method has been confirmed in two metrics, PIQE and NIQE, except with the BRISQUE metric, which recorded a small effect. However, AFGP still outperformed since the d-estimated of all matrices falls into the bounds of the confidence intervals.

## V. CONCLUSION

This study presents an adapted FGP algorithm for MR image denoising. The algorithm is adequately adjusted to overcome the problem of the original counterpart and provide better quality results deprived of over-smoothing or high blurring by automating the computation of the regularization factor and adding a detail-emphasis step. The AFGP algorithm is tested with various real-noisy images to assess its denoising abilities and then compared against the original and five other algorithms to benchmark its performance. The results are then evaluated using three advanced algorithms in addition to recorded processing speed. Accordingly, the AFGP algorithm performance surpassed the performances of other algorithms while recording low computational times, removing the noise efficiently while retaining the minor details without massively amplifying the blur. As for limitation, we observed that utilizing blurred images as input to our denoising method significantly reduces its efficacy. The blurred MRI images compromise AFGP capacity to achieve precise restoration and enhance image quality. This decline in performance arises due to the blurriness that conceals the important details and structures in the image, thereby posing a challenge for the denoising method to differentiate between noise and authentic anatomical features. Hence, the resulting images frequently need more detail and clarity. The AFGP can be further improved for future development by utilizing advanced mathematical models that help increase the efficiency of noise removal in the presence of blur and reduce the needed iterations to reach the desired results.

## CONFLICT OF INTEREST

The authors confirm that no conflict of interest is involved in this study.

## AUTHOR CONTRIBUTIONS

Manar A. Al-Abaji contributed to the study's data collection, analysis, research design, algorithm

development, and drafting. Zohair Al-Ameen provided amendments and guidance on the utilized methodology, algorithm development, data interpretation, analysis of findings, and article review. All authors had approved the final version.

## REFERENCES

- [1] Y. C. Heo, K. Kim, and Y. Lee, "Image denoising using Non-Local Means (NLM) approach in Magnetic Resonance (MR) imaging: A systematic review," *Appl. Sci.*, vol. 10, Oct. 2020. doi: 10.3390/app10207028
- [2] X. You, N. Cao, H. Lu, M. Mao, and W. Wang, "Denoising of MR images with Rician noise using a wider neural network and noise range division," *Magn. Reson. Imaging*, vol. 64, no. May, pp. 154–159, Dec. 2019. doi: 10.1016/j.mri.2019.05.042
- [3] R. Kala and P. Deepa, "Removal of rician noise in MRI images using bilateral filter by fuzzy trapezoidal membership function," in *Proc. 2017 4th International Conference on Advanced Computing and Communication Systems (ICACCS)*, IEEE, Jan. 2017, pp. 1–6. doi: 10.1109/ICACCS.2017.8014648
- [4] V. H. K. Joshi, "MRI denoising using BM3D equipped with noise invalidation denoising technique and VST for improved contrast," *SN Appl. Sci.*, vol. 2, pp. 1–8, 2020. doi: 10.1007/s42452-020-1937-7
- [5] Z. Al-ameen and G. Sulong, "Attenuating noise from computed tomography medical images using a coefficients-driven total variation denoising algorithm," *Int. J. Imaging Syst. Technol.*, vol. 24, pp. 350–358, 2014. doi: 10.1002/ima.22112
- [6] A. Upadhyaya, P. Sagar, M. Kumar, and S. K. Mishra, "Particle swarm optimization—Functional link multilayer perceptron for rician noise suppression from MRI images," in *Proc. 2016 International Conference on Global Trends in Signal Processing, Information Computing and Communication (ICGTSPICC)*, IEEE, Dec. 2016, pp. 103–107. doi: 10.1109/ICGTSPICC.2016.7955278
- [7] P. K. Mishro, S. Agrawal, R. Panda, and A. Abraham, "A survey on state-of-the-art denoising techniques for brain magnetic resonance images," *IEEE Rev. Biomed. Eng.*, vol. 15, pp. 184–199, 2022. doi: 10.1109/RBME.2021.3055556
- [8] S. Paris, P. Kornprobst, J. Tumblin, and F. Durand, "Bilateral filtering: Theory and applications," *Found. Trends® Comput. Graph. Vis.*, vol. 4, no. 1, pp. 1–75, 2008. doi: 10.1561/06000000020
- [9] A. Beck and M. Teboulle, "Fast gradient-based algorithms for constrained total variation image denoising and deblurring problems," *IEEE Trans. Image Process.*, vol. 18, no. 11, pp. 2419–2434, Nov. 2009. doi: 10.1109/TIP.2009.2028250
- [10] S. Gu, L. Zhang, W. Zuo, and X. Feng, "Weighted nuclear norm minimization with application to image denoising," in *Proc. 2014 IEEE Conference on Computer Vision and Pattern Recognition*, IEEE, Jun. 2014, pp. 2862–2869. doi: 10.1109/CVPR.2014.366
- [11] A. Phophalia and S. K. Mitra, "Rough set based bilateral filter design for denoising brain MR images," *Appl. Soft Comput.*, vol. 33, pp. 1–14, Aug. 2015. doi: 10.1016/j.asoc.2015.04.005
- [12] Q. Guo, C. Zhang, Y. Zhang, and H. Liu, "An efficient SVD-based method for image denoising," *IEEE Trans. Circuits Syst. Video Technol.*, vol. 26, no. 5, pp. 868–880, May 2016. doi: 10.1109/TCSVT.2015.2416631
- [13] T. Adam and R. Paramesran, "Image denoising using combined higher order non-convex total variation with overlapping group sparsity," *Multidimens. Syst. Signal Process.*, vol. 30, no. 1, pp. 503–527, Jan. 2019. doi: 10.1007/s11045-018-0567-3
- [14] I. Frosio and J. Kautz, "Statistical nearest neighbors for image denoising," *IEEE Trans. Image Process.*, vol. 28, no. 2, pp. 723–738, Feb. 2019. doi: 10.1109/TIP.2018.2869685
- [15] U. Erkan, D. N. H. Thanh, L. M. Hieu, and S. Enginoglu, "An iterative mean filter for image denoising," *IEEE Access*, vol. 7, no. November, pp. 167847–167859, 2019. doi: 10.1109/ACCESS.2019.2953924
- [16] D. N. H. Thanh, V. B. S. Prasath, L. M. Hieu, and S. Dvoenko, "An adaptive method for image restoration based on high-order total variation and inverse gradient," *Signal, Image Video Process.*, vol. 14, no. 6, pp. 1189–1197, Sep. 2020. doi: 10.1007/s11760-020-01657-9

- [17] D. Pankaj, D. Govind, and K. A. Narayanankutty, "Biomedical signal processing and control a novel method for removing Rician noise from MRI based on variational mode decomposition," *Biomed. Signal Process. Control*, vol. 69, no. 2021, 102737, 2021. doi: 10.1016/j.bspc.2021.102737
- [18] D. Singh and A. Kaur, "Improved fuzzy based non-local mean filter to denoise rician noise," *Turkish Journal of Computer and Mathematics Education (TURCOMAT)*, vol. 12, no. 7, pp. 2116–2121, 2021.
- [19] H. Chung, E. S. Lee, and J. C. Ye, "MR Image denoising and super-resolution using regularized reverse diffusion," *IEEE Trans. Med. Imaging*, vol. 42, no. 4, pp. 922–934, Apr. 2023. doi: 10.1109/TMI.2022.3220681
- [20] P. S. Srinivasan and P. Gurunathan, "Enriched model of intuitionistic fuzzy adaptive noise filtering on MR brain image," *SN Comput. Sci.*, vol. 4, no. 2, p. 166, Jan. 2023. doi: 10.1007/s42979-022-01591-2
- [21] S. Ahmmmed *et al.*, "Enhancing brain tumor classification with transfer learning across multiple classes: An in-depth analysis," *BioMedInformatics*, vol. 3, no. 4, pp. 1124–1144, 2023. doi: 10.3390/biomedinformatics3040068
- [22] B. Awudong, P. Yakupu, J. Yan, and Q. Li, "Research and implementation of denoising algorithm for brain MRIs via morphological component analysis and adaptive threshold estimation," *Mathematics*, vol. 12, no. 5, p. 748, Mar. 2024. doi: 10.3390/math12050748
- [23] S. Li, F. Wang, and S. Gao, "New non-local mean methods for MRI denoising based on global self-similarity between values," *Comput. Biol. Med.*, vol. 174, no. March, 108450, 2024. doi: 10.1016/j.compbiomed.2024.108450
- [24] Z. F. Pang, Y.-M. Zhou, T. Wu, and D.-J. Li, "Image denoising via a new anisotropic total-variation-based model," *Signal Process. Image Commun.*, vol. 74, no. February, pp. 140–152, May 2019. doi: 10.1016/j.image.2019.02.003
- [25] N. Venkatanath, D. Praneeth, M. Chandrasekhar Bh, S. S. Channappayya, and S. S. Medasani, "Blind image quality evaluation using perception based features," in *Proc. 2015 Twenty First National Conference on Communications (NCC)*, Mumbai, India: IEEE, Feb. 2015, pp. 1–6. doi: 10.1109/NCC.2015.7084843
- [26] T. Sun, X. Zhu, J.-S. Pan, J. Wen, and F. Meng, "No-reference image quality assessment in spatial domain," *Genetic and Evolutionary Computing*, vol. 21, no. 12, 2015, pp. 381–388. doi: 10.1007/978-3-319-12286-1\_39
- [27] A. Mittal, R. Soundararajan, and A. C. Bovik, "Making a 'Completely blind' image quality analyzer," *IEEE Signal Process. Lett.*, vol. 20, no. 3, pp. 209–212, Mar. 2013. doi: 10.1109/LSP.2012.2227726
- [28] B. Wang, B. Zhao, C. Deng, and L. Tang, "Adaptive parameter estimation for total variation image denoising," in *Proc. 2013 IEEE International Symposium on Circuits and Systems (ISCAS2013)*, IEEE, May 2013, pp. 2832–2835. doi: 10.1109/ISCAS.2013.6572468

Copyright © 2025 by the authors. This is an open access article distributed under the Creative Commons Attribution License ([CC-BY-4.0](https://creativecommons.org/licenses/by/4.0/)), which permits use, distribution and reproduction in any medium, provided that the article is properly cited, the use is non-commercial and no modifications or adaptations are made.